

# Construction of semi-dynamic model of subduction zone with given plate kinematics in 3D sphere

M. Morishige<sup>1</sup>, S. Honda<sup>1</sup>, and P. J. Tackley<sup>2</sup>

<sup>1</sup>Earthquake Research Institute, the University of Tokyo, 1-1-1 Yayoi, Bunkyo-ku, Tokyo 113-0032, Japan

<sup>2</sup>Institute of Geophysics, NO H9.1 ETH Zurich CH-8092, Zurich, Switzerland

(Received May 31, 2010; Revised September 17, 2010; Accepted September 28, 2010; Online published December 13, 2010)

We present a semi-dynamic subduction zone model in a three-dimensional spherical shell. In this model, velocity is imposed on the top surface and in a small three-dimensional region around the shallow plate boundary while below this region, the slab is able to subduct under its own weight. Surface plate velocities are given by Euler's theorem of rigid plate rotation on a sphere. The velocity imposed in the region around the plate boundary is determined so that mass conservation inside the region is satisfied. A kinematic trench migration can be easily incorporated in this model. As an application of this model, mantle flow around slab edges is considered, and we find that the effect of Earth curvature is small by comparing our model with a similar one in a rectangular box, at least for the parameters used in this study. As a second application of the model, mantle flow around a plate junction is studied, and we find the existence of mantle return flow perpendicular to the plate boundary. Since this model can naturally incorporate the spherical geometry and plate movement on the sphere, it is useful for studying a specific subduction zone where the plate kinematics is well constrained.

**Key words:** Semi-dynamic model, subduction zone, 3D sphere, mantle flow.

## 1. Introduction

Roughly speaking, there are two types of approaches to modeling subduction zones. One is to impose the velocity and the geometry of the plate in advance, an approach that has been used for a long time (e.g., McKenzie, 1969; Kneller and van Keken, 2007, 2008). The other is to calculate slab movement more or less dynamically (e.g., Billen *et al.*, 2003; Billen and Hirth, 2005; Schellart *et al.*, 2007; Morra *et al.*, 2009). Both approaches have advantages and disadvantages. Conceptually, fully dynamic models are undoubtedly preferable but this approach is justified only when we know the rheology of plate well enough. In addition, even if we know such a rheology, it is often difficult to apply this model to the specific subduction zone, since we cannot control the velocity and geometry of subduction zones. However, it is a useful technique to study the general characteristics of subduction zones.

On the other hand, using the kinematic approach, we can construct models that incorporate the present velocity and geometry of specific subduction zones to compare the models with observations. The demerit is that this kind of model may miss some important dynamics of subduction, such as the change in plate boundaries and trench curvature with time (Schellart *et al.*, 2007). Thus, we believe that these two types of approaches are complementary to each other and that an understanding of both type of approaches will lead to further understanding of subduction zones.

The philosophy of imposing velocity on some part is not as novel as mentioned above. But, in reality, it is not so easy to construct models based on it because it is difficult to find an appropriate velocity distribution to impose. Because of simpleness, this type of model has been constructed in the two-dimensional (2D) case since the early days of plate tectonics, but 3D modeling is a recent development (e.g., Kneller and van Keken, 2007, 2008; Honda, 2009). Kneller and van Keken (2007, 2008) imposed the velocity of the whole subducting plate in a rectangular box to study the 3D flow of the curved subduction zone. Honda (2008, 2009) constructed a model somewhat between kinematic and dynamic models in a rectangular box. The velocity on the surface and the small region surrounding a shallow plate boundary are given a priori. The velocity imposed in the plate boundary region is determined so that mass conservation inside the region is satisfied under the assumption that the relative velocity of oceanic subregion with respect to continental subregion is parallel to the plate boundary. Deeper flow is affected by the slab density. The model can include the trench migration kinematically.

In this paper, we show that we can extend the same concept of Honda (2008, 2009) to more realistic geometry (i.e., cylindrical and spherical geometry) and show some examples of the applications for the case of spherical geometry.

## 2. General Model Descriptions

### 2.1 Basic equations

The basic equations used in this study are common in the field of mantle convection studies. Under the assumptions of an incompressible viscous fluid, negligible inertia and the Boussinesq approximation, the basic equations to be

Copyright © The Society of Geomagnetism and Earth, Planetary and Space Sciences (SGEPSS); The Seismological Society of Japan; The Volcanological Society of Japan; The Geodetic Society of Japan; The Japanese Society for Planetary Sciences; TERRAPUB.

Table 1. The symbol used in this study and its meaning and value.

Symbol	Meaning	Value
$v$	Velocity	
$v_i$	$i$ -component of velocity	
$\underline{\underline{\tau}}(\tau_{ij})$	Deviatric stress tensor	
$p$	Pressure	
$\rho$	Density	
$g$	Gravitational acceleration	10 m/s <sup>2</sup>
$\underline{e}_i$	Unit vector in $i$ -direction	
$\eta$	Viscosity	
$\rho_0$	Reference density	4000 kg/m <sup>3</sup>
$\alpha$	The coefficient of thermal expansion	$3 \times 10^{-5}$ /K
$T$	Temperature	
$\kappa$	Thermal diffusivity	$10^{-6}$ m <sup>2</sup> /s
$\omega_A$	Angular velocity of plate A	See text.
$\omega_B$	Angular velocity of plate B	See text.
$V_{AS}$	Speed of plate A at $\theta = 90^\circ$ in spherical geometry	See text.
$V_{BS}$	Speed of plate B at $\theta = 90^\circ$ in spherical geometry	See text.
$\underline{V}_C$	Velocity component on the continental subregion	See text.
$\underline{V}_O$	Velocity component on the oceanic subregion	See text.
$r_0$	Minimum $r$ of the boundary region	See text.
$r_1$	Maximum $r$ of the boundary region	See text.
$\theta_0$	Minimum $\theta$ of the boundary region	See text.
$\theta_1$	Maximum $\theta$ of the boundary region	See text.
$\phi_0$	Minimum $\phi$ of the boundary region	See text.
$\phi_1$	Maximum $\phi$ of the boundary region	See text.
$\Delta r$	Radial distance of a finite volume	See text.
$\Delta \theta$	Inclination of a finite volume	See text.
$\Delta \phi$	Azimuth of a finite volume	See text.
$\phi_{\text{trench}}$	The position of trench	See text.
$\eta_0$	Reference viscosity	See text.
$E$	Activation energy	210 kJ/mol
$R$	Gas constant	8.314 J/K/mol

solved are given by (the meanings of symbols and physical properties are summarized in Table 1),

$$\nabla \cdot \underline{v} = 0 \quad (\text{Mass conservation}) \quad (1)$$

$$\nabla \cdot \underline{\underline{\tau}} - \nabla p = -\rho g \underline{e}_z \quad (\text{Equation of motion}), \quad (2)$$

$$\underline{\underline{\tau}} = \eta \{ (\nabla \underline{v}) + (\nabla \underline{v})^T \} \quad (\text{Constitutive relation}), \quad (3)$$

$$\rho = \rho_0(1 - \alpha T) \quad (4)$$

(Equation of state: Boussinesq approximation),

$$\frac{\partial T}{\partial t} + \underline{v} \cdot \nabla T = \kappa \nabla^2 T \quad (5)$$

(Energy equation with constant thermal conductivity and no internal heating).

These equations are discretized using finite volumes and they are solved by the program StagYY (Tackley, 2008) which is modified to include plate-like features as described below. Other details are described in the section of examples.

## 2.2 Implementation of subduction-like features

In the following discussion, the ‘‘north’’ of the spherical coordinate system corresponds to the axis of rotation and the convergence of each plate is perpendicular to longitude, that is, the axes of both plate rotations are the same.

In order for the slab to subduct at a given angle in the  $r$  (radius)- $\phi$  (longitude) plane, we impose the velocity inside a small region around shallow plate boundary, which we hereafter call the ‘boundary region’ (Fig. 1). Figure 1 shows a  $\theta$  (colatitude)—slice of the boundary region and its surroundings. The top surface is divided into two plates (plates A and B), and each plate velocity is constrained by the rigid rotation given by

$$\begin{cases} \underline{V}_A = r_1 \omega_A \sin \theta \underline{e}_\phi = V_{AS} \sin \theta \underline{e}_\phi \\ \underline{V}_B = r_1 \omega_B \sin \theta \underline{e}_\phi = V_{BS} \sin \theta \underline{e}_\phi \end{cases}, \quad (6)$$

where  $r_1$  is the radius of the Earth,  $\theta$  is the colatitude measured from the north pole,  $\omega_A$  and  $\omega_B$  are the angular velocities of plates A and B, respectively.  $V_{AS}(= r_1 \omega_A)$  and  $V_{BS}(= r_1 \omega_B)$  are the surface speeds at  $\theta = 90^\circ$  of the plates A and B, respectively. Equation (6) means that we can naturally incorporate the variation of plate velocity along the trench by considering spherical geometry.

The velocity inside the boundary region is determined as follows. The boundary region can be divided into two subregions: the continental subregion (upper right region of Fig. 1) and the oceanic subregion (lower left region of Fig. 1). Defining  $\underline{V}_C$  and  $\underline{V}_O$  as the velocity inside each subregion, we assume that their horizontal components are

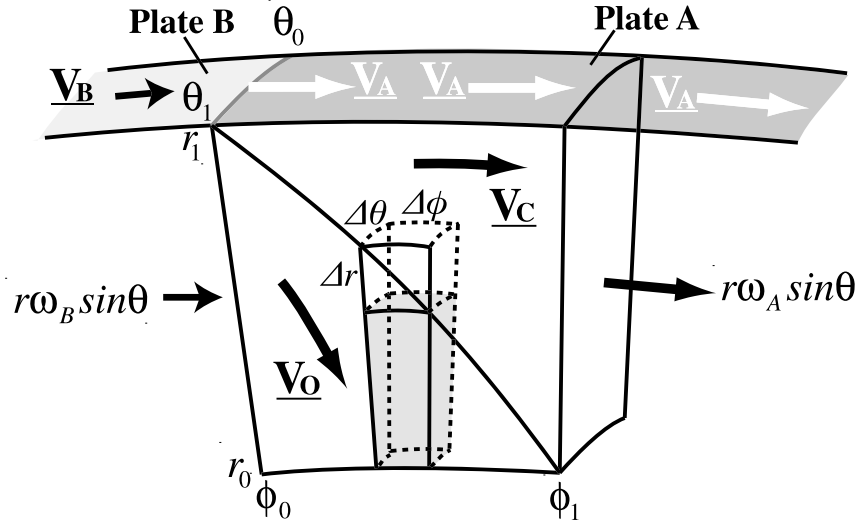


Fig. 1. Schematic view of the boundary region around the trench. The region extends from  $r_0$  to  $r_1$  ( $r$ -direction), from  $\theta_0$  to  $\theta_1$  ( $\theta$ -direction), and from  $\phi_0$  to  $\phi_1$  ( $\phi$ -direction). The region is divided into two subregions (oceanic subregion and continental subregion) and a different velocity is imposed on each subregion ( $V_O$  for oceanic subregion and  $V_C$  for continental subregion). A finite volume whose size is  $\Delta r$  ( $r$ -direction)  $\times \Delta \theta$  ( $\theta$ -direction)  $\times \Delta \phi$  ( $\phi$ -direction) and whose center is on the boundary ( $r_{PB}$ ,  $\theta_{PB}$ ,  $\phi_{PB}$ ) is also shown.

those of the rigid body rotation associated with each plate movement  $r\omega_A \sin \theta$  (continental subregion) and  $r\omega_B \sin \theta$  (oceanic subregion) where  $r$  is the radius. It may be a good first order approximation to assume that the radial (vertical) component of  $V_C$  is zero, that is, the continental plate cannot subduct. Thus,  $\underline{V}_C$  and  $\underline{V}_O$  are expressed as

$$\begin{cases} \underline{V}_C = r\omega_A \sin \theta \underline{e}_\phi \\ \underline{V}_O = V_r \underline{e}_r + r\omega_B \sin \theta \underline{e}_\phi \end{cases}, \quad (7)$$

where  $V_r$  is  $r$ -component of  $\underline{V}_O$ . In order to determine  $V_r = V_r(r, \theta, \phi)$ , mass conservation is considered. Note that mass conservation in the continental subregion is already satisfied by the above equation. The plate boundary is placed so that it passes the vertex as

$$r_{PB} = \frac{r_0 - r_1}{\phi_1 - \phi_0} (\phi_{PB} - \phi_1) + r_0, \quad (8)$$

where  $(r_i, \phi_i)$  ( $i = 0, 1$ ) is the radial and longitudinal coordinate that characterizes the size of the boundary region, and the subscript 'PB' implies the plate boundary.

First, we consider mass conservation in the finite volume along the plate boundary. The plate boundary is required to intersect all the finite volumes along the plate boundary at their vertices, which means that the number of finite volumes in the 'boundary region' is the same in the  $r$ - and  $\phi$ -directions. This means that the shape of the finite volumes in the 'boundary region' determines the subduction angle imposed. Consider one of those finite volumes as shown in Fig. 1. Considering that the velocity is uniform on each plane of the volume, mass conservation in this volume, whose size is  $\Delta r$  (radius)  $\times \Delta \theta$  (colatitude)  $\times \Delta \phi$  (longitude), is given by

$$\begin{aligned} (r_{PB}\omega_A \sin \theta_{PB})r_{PB}\Delta r\Delta \theta &= (r_{PB}\omega_B \sin \theta_{PB})r_{PB}\Delta r\Delta \theta \\ &+ V_{r,PB}(r_{PB} - \Delta r/2, \theta_{PB}, \phi_{PB})(r_{PB} - \Delta r/2)^2 \\ &\cdot 2 \sin \theta_{PB} \sin(\Delta \theta/2)\Delta \phi, \end{aligned} \quad (9)$$

which gives

$$\begin{aligned} V_{r,PB}(r_{PB} - \Delta r/2, \theta_{PB}, \phi_{PB}) \\ = \frac{r_{PB}^2}{(r_{PB} - \Delta r/2)^2} \frac{\Delta r}{\Delta \phi} \frac{\Delta \theta}{2 \sin(\Delta \theta/2)} (\omega_A - \omega_B). \end{aligned} \quad (10)$$

Below this plate boundary shown by the shadowed area in Fig. 1, we consider only the mass balance in the radial direction since the horizontal component of the velocity does not change with  $\phi$ . This is given by

$$\begin{aligned} V_r(r, \theta_{PB}, \phi_{PB})r^2 \\ = V_{r,PB}(r_{PB} - \Delta r/2, \theta_{PB}, \phi_{PB})(r_{PB} - \Delta r/2)^2 \end{aligned} \quad (11)$$

or

$$\begin{aligned} V_r(r, \theta_{PB}, \phi_{PB}) &= \left( \frac{r_{PB} - \Delta r/2}{r} \right)^2 \\ &\cdot V_{r,PB}(r_{PB} - \Delta r/2, \theta_{PB}, \phi_{PB}). \end{aligned} \quad (12)$$

This is because the area perpendicular to the radial direction is proportional to  $r^2$ .

Finally, from Eqs. (8), (10) and (12), we have

$$\begin{aligned} V_r(r, \theta, \phi) &= \left\{ \frac{\frac{r_0 - r_1}{\phi_1 - \phi_0} (\phi - \phi_1) + r_0}{r} \right\}^2 \\ &\cdot \frac{\Delta r}{\Delta \phi} \frac{\Delta \theta}{2 \sin(\Delta \theta/2)} (\omega_A - \omega_B). \end{aligned} \quad (13)$$

Therefore, the velocity imposed in the boundary region

is given by

$$\left\{ \begin{array}{l} \underline{V_C} = r\omega_A \sin\theta \underline{e_\phi} \\ \underline{V_O} = \left\{ \frac{r_0 - r_1}{\phi_1 - \phi_0} (\phi - \phi_1) + r_0 \right\}^2 \\ \quad \cdot \frac{\Delta r}{\Delta\phi} \frac{\Delta\theta}{2 \sin(\Delta\theta/2)} (\omega_A - \omega_B) \underline{e_r} \\ \quad + r\omega_B \sin\theta \underline{e_\phi} \end{array} \right. . \quad (14)$$

In the limit of infinitesimally small  $\Delta r$ ,  $\Delta\theta$  and  $\Delta\phi$ , this reduces to

$$\left\{ \begin{array}{l} \underline{V_C} = r\omega_A \sin\theta \underline{e_\phi} \\ \underline{V_O} = \left\{ \frac{r_0 - r_1}{\phi_1 - \phi_0} (\phi - \phi_1) + r_0 \right\}^2 \\ \quad \cdot \frac{r_1 - r_0}{\phi_1 - \phi_0} (\omega_A - \omega_B) \underline{e_r} + r\omega_B \sin\theta \underline{e_\phi} \end{array} \right. . \quad (15)$$

Note that Eq. (15) also means that, at the plate boundary, the relative velocity of the oceanic subregion viewed from the continental plate is parallel to the direction of the plate boundary. Based on the same concept, we can also obtain the velocity in the boundary region in cylindrical geometry as

$$\left\{ \begin{array}{l} \underline{V_C} = r\omega_A \underline{e_\phi} \\ \underline{V_O} = \frac{r_0 - r_1}{\phi_1 - \phi_0} (\phi - \phi_1) + r_0 \\ \quad \cdot \frac{r_1 - r_0}{\phi_1 - \phi_0} (\omega_A - \omega_B) \underline{e_r} + r\omega_B \underline{e_\phi} \end{array} \right. , \quad (16)$$

where the velocity of plate A and B are expressed as

$$\left\{ \begin{array}{l} \underline{V_A} = r_1\omega_A \underline{e_\phi} \\ \underline{V_B} = r_1\omega_B \underline{e_\phi} \end{array} \right. . \quad (17)$$

Thus, this method is considered to be a natural extension of that used by Honda (2008, 2009) in a rectangular geometry.

The position of the trench, defined by the surface expression of plate boundary and expressed as an arbitrary function of  $\theta$ ,  $\phi_{\text{trench}}(\theta, t)$ , moves in the  $\phi$ -direction as

$$\phi_{\text{trench}}(\theta, t) = \phi_{\text{trench}}(\theta, 0) + \omega_A t. \quad (18)$$

### 3. Examples

#### 3.1 Flow around slab edges: convergent-transform fault boundary

**3.1.1 Model** As a first example of application of the model, flow around slab edges, that is, a convergent-transform fault boundary as studied by Honda (2009) for

a rectangular box, is considered. A schematic view of the model is shown in Fig. 2(a). The model is tuned to be similar to that of Honda (2009), and it covers the region  $5370 \leq r$  (km)  $\leq 6370$ ,  $85.5 \leq \theta$  ( $^\circ$ )  $\leq 94.5$ ,  $-13.5 \leq \phi$  ( $^\circ$ )  $\leq 13.5$ . Thus a depth extent of 1000 km and a horizontal extent of about 3000 km ( $\phi$ -direction)  $\times$  1000 km ( $\theta$ -direction) is considered. Initially, the trench is located at  $\phi = 0^\circ$  and  $90 \leq \theta$  ( $^\circ$ )  $\leq 94.5$ , and the transform fault is located at  $-13.5 \leq \phi$  ( $^\circ$ )  $\leq 0$  and  $\theta = 90^\circ$ . The size of the boundary region is 100 km ( $r$ -direction)  $\times$   $4.5^\circ$  ( $\theta$ -direction)  $\times$   $0.9^\circ$  ( $\phi$ -direction), and this means that the angle of subduction near the surface is  $\sim 45^\circ$ . The top boundary condition for temperature is  $T = 0$ . The bottom boundary conditions for velocity and temperature are permeable ( $v_\theta = v_\phi = 0$  and  $\tau_{rr} = 0$ ) and no vertical conductive heat flux ( $\partial T / \partial r = 0$ ), respectively. The boundary condition on the walls perpendicular to the  $\theta$ -direction is impermeable free slip for velocity and no horizontal conductive heat flux for temperature ( $v_\theta = \tau_{\theta\phi} = \tau_{r\theta} = 0$ ,  $\partial T / \partial \theta = 0$ ). The boundary condition on the walls perpendicular to the  $\phi$  direction is  $v_r = v_\theta = \partial p / \partial \phi = 0$  for velocity and pressure, and no horizontal conductive heat flux ( $\partial T / \partial \phi = 0$ ) for temperature. These boundary conditions are equivalent to those of Honda (2009) for a rectangular box. The Newtonian viscosity  $\eta$  is given by

$$\eta = \eta_0 h(r) \exp\left(\frac{E}{R(T + 273)}\right), \quad (19)$$

where

$$h(r) = \begin{cases} 1 & (5960 < r \text{ (km)} \leq 6370) \\ 10 & (5710 < r \text{ (km)} \leq 5960) \\ 100 & (5370 \leq r \text{ (km)} \leq 5710) \end{cases} \quad (20)$$

and  $\eta_0$  is set such that the viscosity at  $T = 1300^\circ\text{C}$  is  $10^{20}$  Pa·s with  $h = 1$  (Honda, 2009). The maximum and minimum viscosity are set to  $10^{17}$  Pa·s and  $10^{23}$  Pa·s, respectively. The initial temperature is given by a half-space cooling model, that is,

$$T = T_m \operatorname{erf}\left(\frac{z}{2\sqrt{\kappa t_{\text{age}}}}\right), \quad (21)$$

where  $z$  is the depth and  $T_m = 1300^\circ\text{C}$ .  $t_{\text{age}}$  is set to 25 Myr (under the plate A) and 120 Myr (under the plate B).

The number of finite volumes used is 128 ( $r$ -direction)  $\times$  128 ( $\theta$ -direction)  $\times$  384 ( $\phi$ -direction). Resolution tests have been performed for a 2D model. It is desirable to check the effect of resolution in three dimensions. However, since a 3D calculation with higher resolution requires an impractical amount of computer time, we made tests for a 2D model. Since the geometry of our model is complex, we used a simple successive overrelaxation method to solve the equations of motion. Figure 3 shows the effect of resolution on the results. The number of finite volumes used in the calculation shown in Fig. 3(b) is doubled in both the  $r$ - and  $\phi$ -directions ( $256 \times 768$ ) compared to that shown in Fig. 3(a) ( $128 \times 384$ ). Results show that although minor differences can be seen, the overall behavior is similar between these cases. Thus, this supports the adequacy of the resolution used in this study.

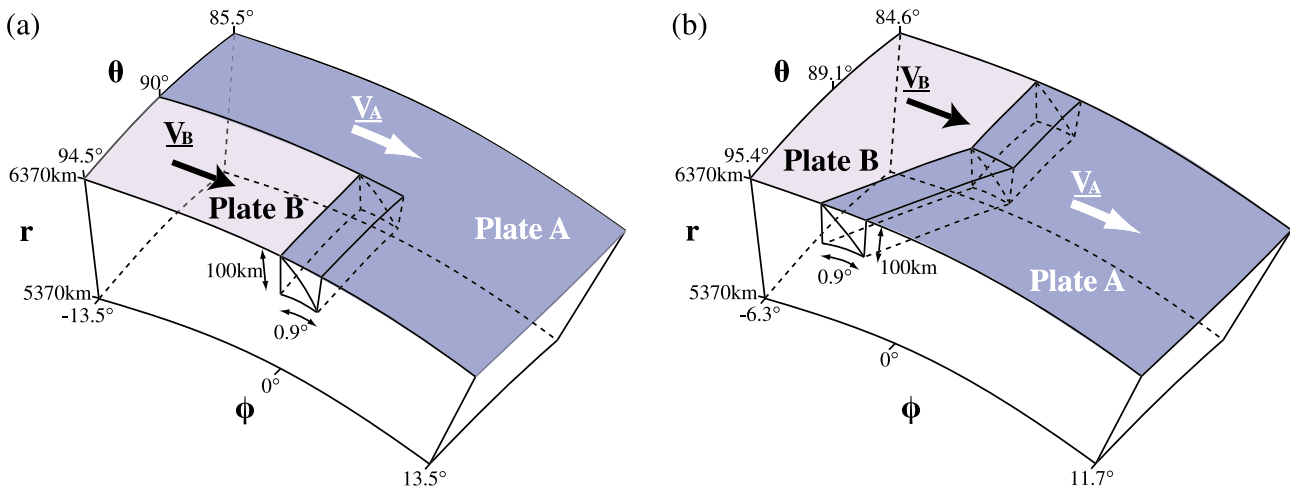


Fig. 2. (a) Schematic view of the model of a convergent-transform fault boundary. The dimension of the region is 1000 km ( $r$ -direction)  $\times$  9° ( $\theta$ -direction)  $\times$  27° ( $\phi$ -direction). The velocities  $V_A$  and  $V_B$  are imposed on the plates A and B, respectively. A detailed view of the boundary region where velocity is imposed is shown in Fig. 1. The dimension of the boundary region is 100 km ( $r$ -direction)  $\times$  4.5° ( $\theta$ -direction)  $\times$  0.9° ( $\phi$ -direction). (b) Schematic view of the model around a plate junction. The dimension of the region is 1000 km ( $r$ -direction)  $\times$  10.8° ( $\theta$ -direction)  $\times$  18° ( $\phi$ -direction).

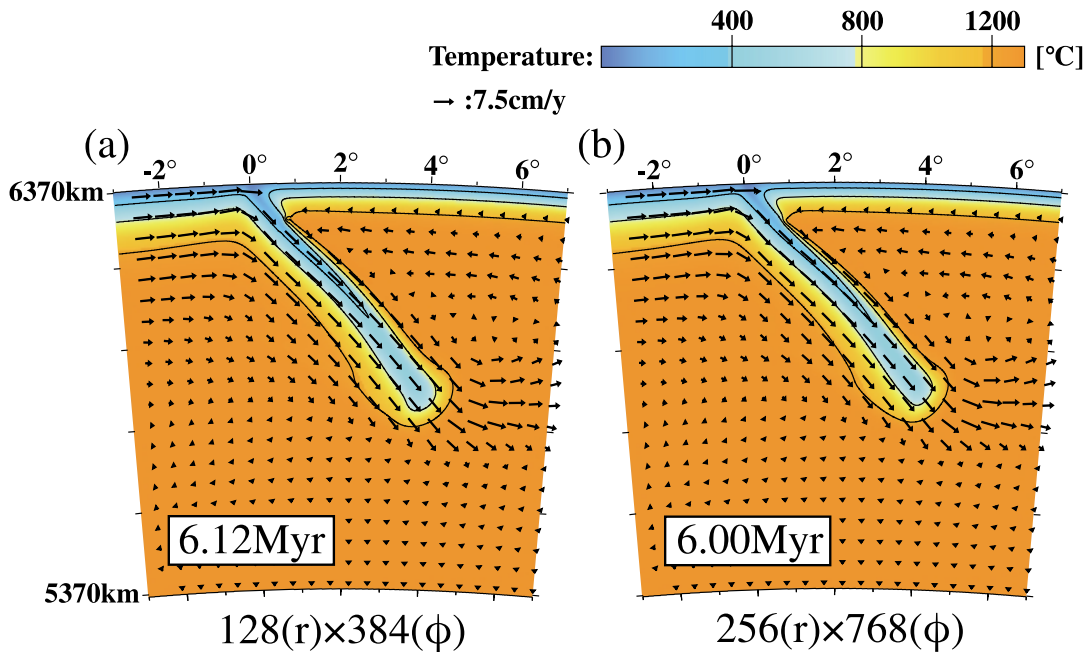


Fig. 3. The effect of the number of finite volumes on results for a 2D case. Temperature and velocity field are shown. The number of finite volumes used is (a) 128 ( $r$ -direction)  $\times$  384 ( $\phi$ -direction) and (b) 256 ( $r$ -direction)  $\times$  768 ( $\phi$ -direction). The time elapsed from the start of calculations is shown on the bottom-left corner of each figure.

**3.1.2 Results** Figure 4 shows the results of three cases with a convergent-transform fault boundary for spherical shell geometry. ( $V_{AS}$ ,  $V_{BS}$ ) used in the calculations in Fig. 4(a, b, c) are (−7.5 cm/y, 0 cm/y), i.e., retreating trench, (0 cm/y, 7.5 cm/y), i.e., fixed trench, and (7.5 cm/y, 15.0 cm/y), i.e., advancing trench, respectively. We can see from this figure that the subduction angle becomes gentler as the trench retreats, and it becomes steeper as the trench advances.

Figure 5 shows cross-sectional views at depths of 200 and 400 km for the cases of retreating trench (Fig. 5(a)), fixed trench (Fig. 5(b)), and advancing trench (Fig. 5(c)). Only the regions around the subducting slab are shown. We

can see that the thickness of slab in the cross section differs in these three cases because of the difference in subduction angle, as seen in Fig. 4.

The slab edge flow shown in Fig. 5 is interesting in terms of the existence/non-existence of along-arc flow in the sub-slab mantle (e.g., Long and Silver, 2008). Honda (2009) first reported the results of this type of model and showed that significant along-arc flow in the sub-slab mantle does not exist unless the trench retreat is large. Comparing the results shown in Fig. 5(a, c) with the corresponding case in a rectangular box (see figures 2 and 3 in Honda (2009)), we can see that the horizontal flow around slab edges in spherical geometry is similar to that in a rectangular box,

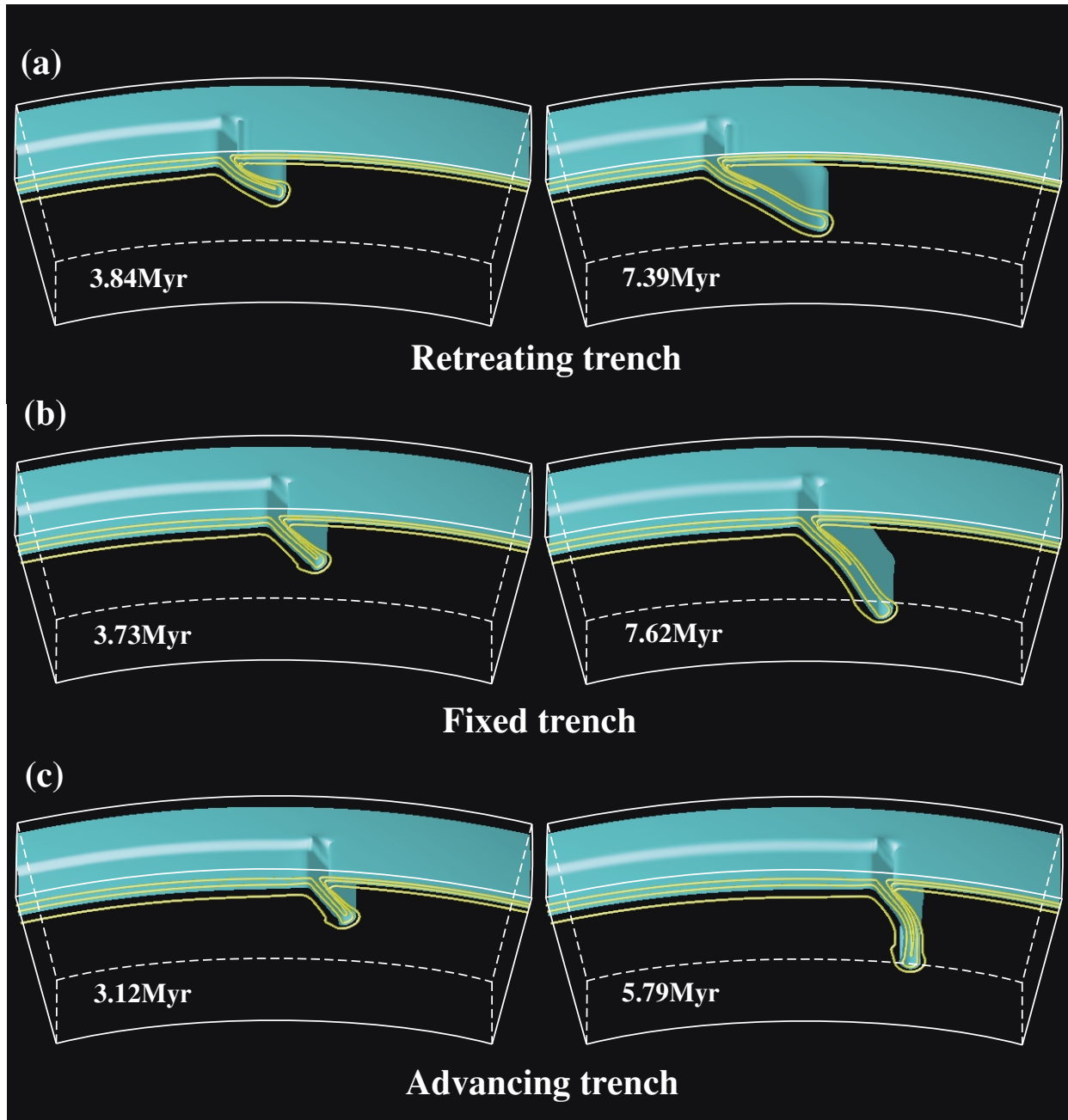


Fig. 4. Temperature structure around slab edges. (a) The case with a retreating trench ( $V_{AS} = -7.5$  cm/yr,  $V_{BS} = 0$  cm/yr). (b) The case with a fixed trench ( $V_{AS} = 0$  cm/yr,  $V_{BS} = 7.5$  cm/yr). (c) The case with an advancing trench ( $V_{AS} = 7.5$  cm/yr,  $V_{BS} = 15.0$  cm/yr). The cyan plane shows an isothermal surface of  $1000^{\circ}\text{C}$ . Yellow lines shows the isotherms of  $400$ ,  $800$ , and  $1200^{\circ}\text{C}$  on the plane with  $\theta = 94.5^{\circ}$ . Time shown in the bottom-left corner of each figure is the time elapsed from the start of each calculation.

which means the effect of Earth curvature on horizontal flow is small, at least for the parameters considered in this study.

### 3.2 Flow around a plate junction

**3.2.1 Model** As a second example of the application of the model, we consider the flow around a plate junction with a fixed trench in a spherical shell. A schematic view of the model is shown in Fig. 2(b). Only the model region and trench position are different from the previous example, and other physical properties, such as viscosity, boundary, and initial conditions, are the same. The dimension of the model region is  $5370 \leq r(\text{km}) \leq 6370$ ,  $84.6 \leq \theta(^{\circ}) \leq 95.4$ ,  $-6.3 \leq \phi(^{\circ}) \leq 11.7$ , and the position of trench in  $\phi$ -

direction  $\phi_{\text{trench}}(\theta)$  is given by

$$\phi_{\text{trench}}(\theta) = \begin{cases} 0^{\circ} & \text{at } 84.6 \leq \theta(^{\circ}) \leq 89.1 \\ (89.1 - \theta)^{\circ}/1.2 & \text{at } 89.1 \leq \theta(^{\circ}) \leq 95.4 \end{cases}, \quad (22)$$

which means that the angle between the strike of the trench and the direction of plate velocity at  $89.1 \leq \theta(^{\circ}) \leq 95.4$  is nearly  $50^{\circ}$ . (Note that it is not necessary for the position of the trench to be a linear function of  $\theta$ ; it could be arbitrary.) The size of boundary region is  $100$  km ( $r$ -direction)  $\times$   $0.9^{\circ}$  ( $\phi$ -direction) for each  $\theta$ . The number of finite volumes

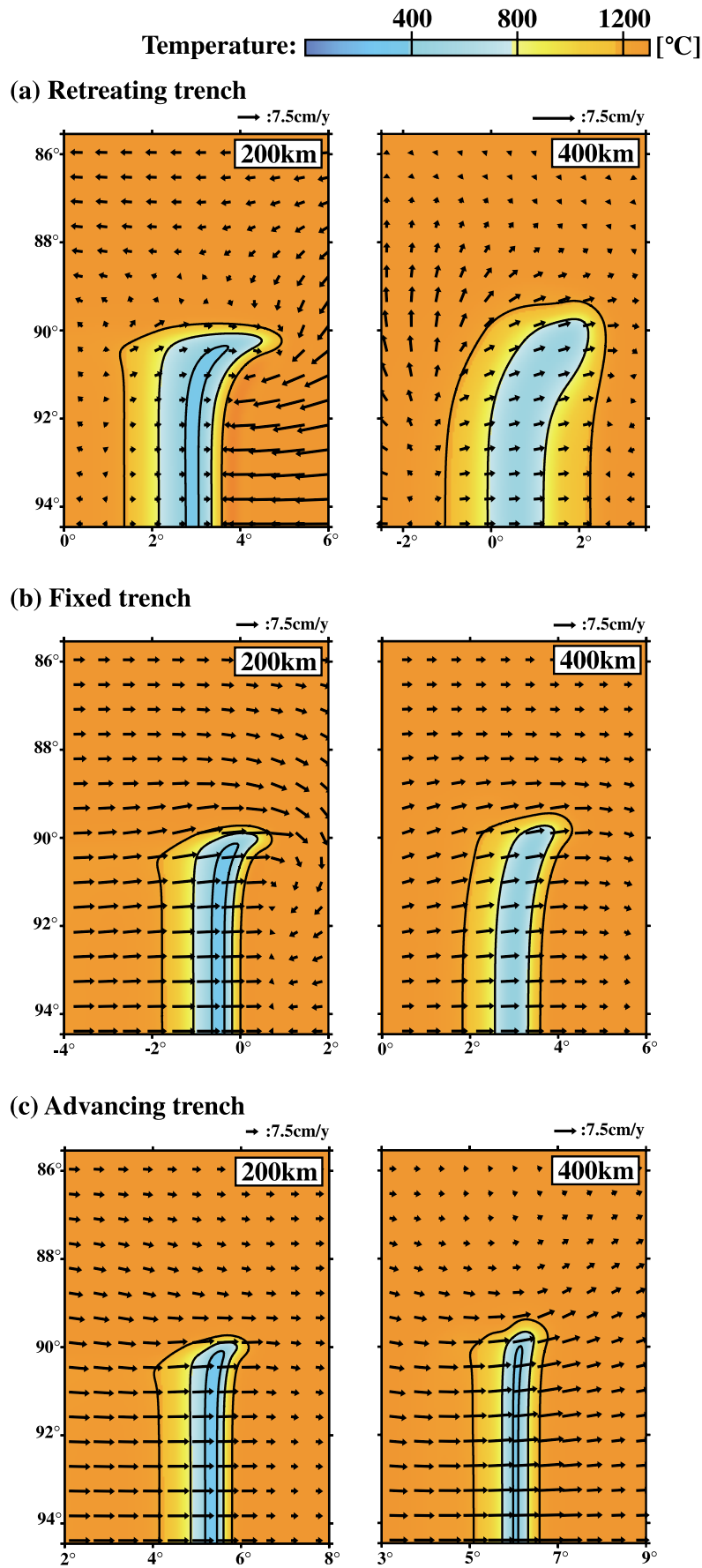


Fig. 5. Horizontal view at depths of 200 and 400 km of flow around the slab edges for the cases of (a) retreating trench, (b) fixed trench and (c) advancing trench. Temperature and velocity fields are shown in the area near the subducting slab. An equidistant cylindrical projection is used. Note that the scale of the velocity vectors is different in each figure. The time elapsed from the start of calculations is (a) 7.39 Myr, (b) 7.62 Myr, and (c) 5.79 Myr, respectively.

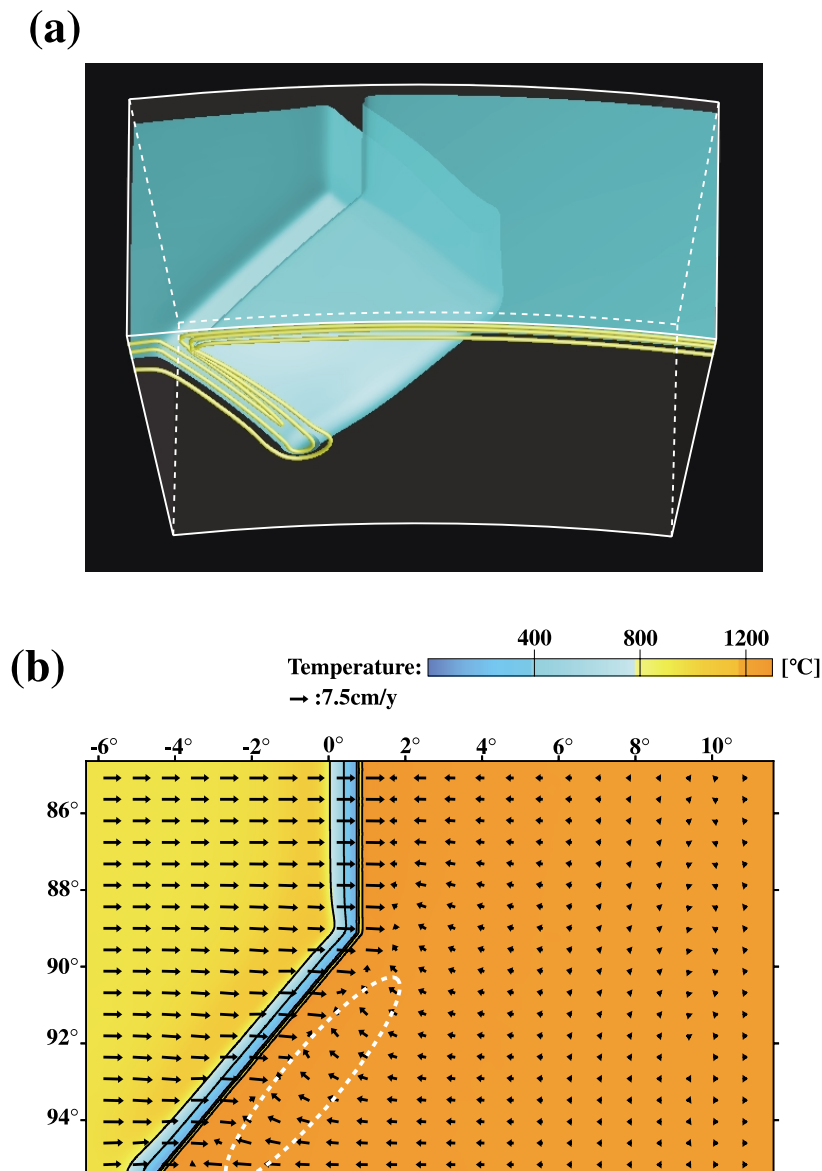


Fig. 6. Flow and temperature around a plate junction. (a) 3D image of the temperature field. The cyan plane shows an isothermal surface of 1000°C. Yellow lines shows isotherms of 400, 800, and 1200°C on the plane with  $\theta = 95.4^\circ$ . (b) Horizontal view at a depth of 100 km of (a). An equidistant cylindrical projection is used. Temperature and velocity fields are shown. Flow perpendicular to the plate boundary exists in the area enclosed by the white dotted line. The time elapsed from the start of calculation is 7.02 Myr.

used is  $128$  ( $r$ -direction)  $\times$   $128$  ( $\theta$ -direction)  $\times$   $256$  ( $\phi$ -direction).

**3.2.2 Results** Figure 6 shows that the resulting temperature and velocity structure. ( $V_{AS}$ ,  $V_{BS}$ ) used in this study is (0 cm/y, 7.5 cm/y). Figure 6(a) shows the 3D temperature field and Fig. 6(b) shows a horizontal view at a depth of 100 km. Interestingly, we see that there is a flow perpendicular to the plate boundary in the area enclosed by white dashed line, and the magnitude of this velocity component is much larger than that of radial velocity component. Similar flow is also reported by Kneller and van Keken (2008) in 3D rectangular geometry.

Nakajima *et al.* (2006) examined the fast directions of shear-wave splitting near the plate junction of the southwestern part of the Kurile arc and the northeastern Japan arc. From their analysis, they suggested that mantle return flow occurs sub-parallel to the local maximum dip of the

slab. The result shown in Fig. 6 may support their inference. However, further systematic study, such as the estimate of seismic anisotropy (e.g., Kneller and van Keken, 2007, 2008) is necessary.

#### 4. Discussion and Conclusion

In this paper, we have constructed a semi-dynamic subduction zone model in a 3D spherical shell and shown some applications. Our model enables the slab to subduct by imposing velocities in a small boundary region so that the number of finite volumes needed is smaller than that required for a complex slab rheology to achieve subduction-like features, such as the narrow low viscosity shear zone (Billen and Hirth, 2005). Additionally, the model can easily incorporate observations such as the geometry of the shallow part of the slab and plate boundary. The model can also include the over-riding plate, which is not considered

in the “free subduction” model (e.g., Schellart *et al.*, 2007; Morra *et al.*, 2009) but is sometimes important (Yamato *et al.*, 2009). However, the model also has a number of limitations, such as an inability to handle more than two plates. In this study, we assume that the pole of both plate motions coincides, although this is not true in general. In theory, such a case could be handled by splitting the plate motion into the motion relative to the reference plate and the absolute motion of the reference plate. In practice, however, this will make the calculations difficult because of the complex boundary conditions. Despite these difficulties, our model is useful for understanding the character of subduction zones and can be applied for a particular pair of plates, such as the Pacific plate and slowly moving Eurasia plate.

It is obvious that our model is better on the point that this uses a 3D sphere, which is the Earth’s geometry, and the effects of Earth curvature can be correctly taken into account. In our examples, we do not see a significant difference between the results in the 3D rectangular box and spherical shell geometry. If, however, we modeled a broader area or deeper processes, such as the deformation of subducted slabs that include the stagnation and the tear in the transition zone and the buckling at the CMB (e.g., Fukao *et al.*, 2001; Loubet *et al.*, 2009; Obayashi *et al.*, 2009), the difference is expected to become more significant, and our model might give a better understanding of such phenomena.

**Acknowledgments.** A part of this work was done, while P. J. T. was a visiting researcher of Earthquake Research Institute, the University of Tokyo. This work was supported by Grant-in-Aid for JSPS Fellows (21-8038) and for Scientific Research (19104011). The Generic Mapping Tools (Wessel and Smith, 1998) were used to draw figures in this study. For this study, we have used the computer systems of the Earthquake Information Center of the Earthquake Research Institute, the University of Tokyo. We thank Masanori Kameyama for his useful comments.

## References

- Billen, M. I. and G. Hirth, Newtonian versus non-Newtonian upper mantle viscosity: Implications for subduction initiation, *Geophys. Res. Lett.*, **32**, L19304, doi:10.1029/2005GL023457, 2005.
- Billen, M. I., M. Gurnis, and M. Simons, Multiscale dynamics of the Tonga-Kermadec subduction zone, *Geophys. J. Int.*, **153**, 359–388, 2003.
- Fukao, Y., S. Widiyantoro, and M. Obayashi, Stagnant slab in the upper and lower mantle transition region, *Rev. Geophys.*, **39**, 291–323, 2001.
- Honda, S., A simple semi-dynamic model of the subduction zone: effects of a moving plate boundary on the small-scale convection under the island arc, *Geophys. J. Int.*, **173**, 1095–1105, 2008.
- Honda, S., Numerical simulations of mantle flow around slab edges, *Earth Planet. Sci. Lett.*, **277**, 112–122, 2009.
- Kneller, E. A. and P. E. van Keken, Trench-parallel flow and seismic anisotropy in the Mariana and Andean subduction systems, *Nature*, **450**, 1222–1226, 2007.
- Kneller, E. A. and P. E. van Keken, Effect of three-dimensional slab geometry on deformation in the mantle wedge: Implications for shear wave anisotropy, *Geochem. Geophys. Geosyst.*, **9**, Q01003, doi:10.1029/2007GC001677, 2008.
- Long, M. D. and P. G. Silver, The subduction zone flow field from seismic anisotropy: A global view, *Science*, **319**, 315–318, 2008.
- Loubet, N., N. M. Ribe, and Y. Gamblin, Deformation modes of subducted lithosphere at the core-mantle boundary: An experimental investigation, *Geochem. Geophys. Geosyst.*, **10**, Q10004, doi:10.1029/2009GC002492, 2009.
- McKenzie, D. P., Speculations on the consequences and causes of plate motions, *Geophys. J. R. Astron. Soc.*, **18**, 1–32, 1969.
- Morra, G., P. Chatelain, P. J. Tackley, and P. Koumoutsakos, Earth curvature effects on subduction morphology: Modeling subduction in a spherical setting, *Acta Geotech.*, **4**, 95–105, 2009.
- Nakajima, J., J. Shimizu, S. Hori, and A. Hasegawa, Shear-wave splitting beneath the southwestern Kurile arc and northeastern Japan arc: A new insight into mantle return flow, *Geophys. Res. Lett.*, **33**, L05305, doi:10.1029/2005GL025053, 2006.
- Obayashi, M., J. Yoshimitsu, and Y. Fukao, Tearing of stagnant slab, *Science*, **324**, 1173–1175, 2009.
- Schellart, W. P., J. Freeman, D. R. Stegman, L. Moresi, and D. May, Evolution and diversity of subduction zones controlled by slab width, *Nature*, **446**, 308–311, 2007.
- Tackley, P. J., Modeling compressible mantle convection with large viscosity contrasts in a three-dimensional spherical shell using the yin-yang grid, *Phys. Earth Planet. Inter.*, **171**, 7–18, 2008.
- Wessel, P. and W. H. F. Smith, New improved version of the Generic Mapping Tools released, *Eos Trans. AGU*, **79**, 579, 1998.
- Yamato, P., L. Husson, J. Braun, C. Loiselet, and C. Thieulot, Influence of surrounding plates on 3D subduction dynamics, *Geophys. Res. Lett.*, **36**, L07303, doi:10.1029/2008GL036942, 2009.

M. Morishige (e-mail: stellvia@eri.u-tokyo.ac.jp), S. Honda, and P. J. Tackley